Materials Today Chemistry 53 (2026) 103531

Contents lists available at ScienceDirect

Materials Today Chemistry

journal homepage: www.journals.elsevier.com/materials-today-chemistry/

# Synergistic flame retardancy enabled by boehmite/poly(acrylic acid)/graphene oxide hybrid multilayered nanocomposites

Inyoung Lee [a], Yong Chae Jung [b], Yong Tae Park [c,*], Jung Sang Cho [d,**], Chungyeon Cho [e,***]

[a] Department of Chemical Engineering, College of Engineering, Wonkwang University, Iksan, 54538, Republic of Korea
[b] Institute of Advanced Composite Materials, Korea Institute of Science and Technology (KIST) 92 Chudong-ro, Bongdong-eup, Wanju-gun, Jeonllabuk-do 55324, Republic of Korea
[c] Division of Mechanical Systems Engineering, Myongji University, 116 Myongji-ro, Cheoin-gu, Yongin, Gyeonggi-do, 17058, Republic of Korea
[d] Department of Engineering Chemistry, Chungbuk National University, Chungbuk, 361-763, Republic of Korea
[e] Department of Biomedical Materials Science, Jeonbuk Advanced Bio-convergence Academy, Wonkwang University, Iksan, Jeonbuk, 54538, Republic of Korea

ARTICLE INFO

*Keywords:*
Layer-by-layer assembly
Boehmite
Graphene oxide
Flame retardants
Polymer nanocomposites

ABSTRACT

We report a sustainable flame retardant (FR) nanocoating fabricated via layer-by-layer (LbL) assembly of boehmite (BMT), poly (acrylic acid) (PAA), and graphene oxide (GO). Introducing a PAA interlayer between inorganic and carbonaceous platelets generates denser and thicker multilayers than conventional bilayer coatings, enabling stronger interfacial interactions and higher nanoparticle loading. These structural features promote robust char formation during combustion, which is critical for enhancing fire resistance. Applied to cotton fabrics and polyurethane foams, the BMT/PAA/GO coatings significantly improve thermal stability, delay degradation, and suppress heat release, as confirmed by thermogravimetric and cone calorimetry analyses. Quantitatively, a 10-cycle BMT/PAA/GO coating (~7.5 wt% add-on) eliminated the second peak heat release rate of polyurethane foam and reduced total smoke release and production by ~ 60%, while increasing high-temperature char yield to ~7.7 wt%. Unlike uncoated controls, the coated substrates largely preserve their structural integrity after flame exposure, demonstrating the barrier effect and char reinforcement imparted by the hybrid layers. This study highlights an aqueous and scalable FR approach, offering a practical pathway toward advanced fire-safety materials for textiles, foams, and related polymer-based applications.

## 1. Introduction

Polymeric materials, including natural cellulose-based cotton and synthetic polyurethane foams (PUF), are indispensable in applications ranging from bedding and interior furnishings to packaging and transportation, owing to their ease of processing and robust mechanical properties [1,2]. However, their high flammability presents serious risks to human health and the environment, making enhanced flame retardancy a persistent challenge [3,4]. Although halogenated flame retardants (FR) have been widely used due to their effectiveness in reducing heat release their tendency to persist in ecosystems and generate toxic byproducts has prompted growing regulatory concern [5–7]. Consequently, research has turned to halogen-free alternatives, such as those based on silicon, nitrogen, phosphorus, or expandable graphite, which aim to maintain fire safety while mitigating ecological impact [8–10]. These developments underscore the pressing need for next-generation FR materials that balance performance with environmental responsibility.

To address these concerns, halogen-free FR strategies have emerged, incorporating phosphorus, nitrogen, silicon-based additives, or carbonaceous systems such as expandable graphite [11–13]. In this context, polymer nanocomposites represent a promising class of materials because their organic–inorganic hybrid structures can simultaneously enhance mechanical, thermal, and barrier properties [14–16]. Inorganic clays (e.g., boehmite (BMT), montmorillonite, vermiculite) and carbon-based fillers (e.g., graphene oxide (GO), carbon nanotubes) have

---

* Corresponding author.
** Corresponding author.
*** Corresponding author.
*E-mail address:* cncho37@wku.ac.kr (C. Cho).

https://doi.org/10.1016/j.mtchem.2026.103531
Received 9 December 2025; Received in revised form 22 February 2026; Accepted 10 March 2026

been especially effective due to their high aspect ratio, thermal stability, and ability to reinforce char formation [17–19]. These fillers can synergistically suppress heat transfer and oxygen diffusion, thereby improving flame retardancy [20–23]. Carbonaceous nanomaterials, including graphene and carbon nanotubes, exhibit high thermal conductivity, mechanical durability, and the capacity to promote protective char layers, thereby enhancing flame retardancy [24–26]. GO is particularly attractive due to its two-dimensional structure decorated with oxygen-containing groups, which facilitates solution-based processing and broad applicability in composites and devices. When combined with inorganic nanoplatelets, these fillers synergistically suppress heat transfer, restrict oxygen diffusion, and reinforce char formation [27,28]. Nevertheless, realizing these advantages requires precise control of the nanocomposite architecture, as poor dispersion and interfacial incompatibility between inorganic fillers and polymer matrices often hinder the development of uniform and densely packed structures [29].

Layer-by-layer (LbL) assembly has emerged as a highly versatile technique for fabricating advanced nanocomposites with precise control over thickness, composition, and function [30]. In this method, substrates are sequentially immersed in aqueous solutions of oppositely charged polyelectrolytes or nanoparticles, producing ultrathin multilayer coatings stabilized by electrostatic interactions, hydrogen bonding, or hydrophobic forces [31–33]. Film properties can be tuned by parameters such as pH, ionic strength, or molecular weight, enabling bilayers with nanometer-to submicrometer-scale thickness [34,35]. Importantly, this aqueous-based strategy preserves the physical integrity of substrates while imparting flame-retardant barriers. LbL films incorporating clays or carbon nanomaterials have been reported to suppress heat and mass transfer during combustion and promote char formation [36,37]. Although some inorganic-based LbL coatings have shown appreciable FR effects, systems without polymer interlayers were still constrained by restricted nanoparticle loading and less compact architectures, while other nanocomposite coatings suffered from poor dispersion and scalability issues, underscoring the need for advanced hybrid designs [38,39].

Despite these advances, critical research gaps remain in the design of LbL-based FR coatings. While several systematically engineered LbL systems have demonstrated outstanding FR performance even with a limited number of layers, simple or weakly integrated layering of nanoclays, GO, or polyelectrolytes has more commonly resulted in limited nanoparticle loading and modest fire protection [40–44]. Furthermore, the potential synergistic role of hydrogen bonding under acidic conditions has rarely been considered. Based on these gaps, we hypothesized that incorporating poly (acrylic acid) (PAA) as an interlayer between cationic BMT and anionic GO would enhance interfacial interactions, increase nanoparticle deposition, and promote denser multilayer growth, ultimately improving FR performance. To validate this hypothesis, we constructed trilayer (TL) coatings consisting of BMT, PAA, and GO, and deposited them on PUF and fabrics. Compared to bilayer (BL) coatings, the TL architecture significantly enhanced flame retardancy, primarily through denser char formation and higher nanoparticle loading. Moreover, deposition at pH 2.5 promotes hydrogen bonding along with electrostatic attraction, reinforcing interfacial cohesion and enhancing the structural integrity of the coatings on polymer-based materials. In contrast to prior LbL FR studies that mainly rely on compositional design, the present work introduces an interlayer-mediated architectural strategy, demonstrating that a polymer interlayer can fundamentally transform multilayer growth mode and associated structure-property relationships. Collectively, this eco-friendly and scalable strategy not only advances fundamental understanding of hybrid multilayer design but also offers broad potential for enhancing fire safety in textiles, foams, and other polymer-based applications.

## 2. Experimental section

### *2.1. Materials and substrates*

PAA (Mw ≈ 100,000 g/mol, 35 wt% in water) and branched polyethylenimine (BPEI; Mw ≈ 25,000 g/mol) were procured from Sigma-Aldrich (Milwaukee, WI, USA). BMT nanopowder ($AlOOH{\cdot}xH_2O$, product no. 1315 TB) was obtained from SkySpring Nanomaterials, Inc. (Houston, TX, USA) and used without further modification. According to the manufacturer's specification, the material exhibits a primary crystallite size of 10-20 nm, a median secondary particle size (D50) of ~170-180 nm, a high specific surface area (~143 $m^2$ $g^{-1}$), and a cationic surface charge in aqueous dispersion. A 1 wt% BMT dispersion was prepared by stirring the nanopowder in deionized (D.I) water for 12 h. Highly concentrated aqueous GO solution (lateral dimensions of ~1-1.5 μm and thickness of ~1-2 nm) was purchased from Graphene Supermarket (Graphene Laboratories Inc., NY, USA) and is characterized by a high oxidation degree (oxygen content: 41-50%, C/O ~ 1.0-1.3) and abundant oxygen-containing functional groups, as confirmed by the manufacturer's XPS data. Although the manufacturer does not provide viscosity or a molecular-weight distribution, previous studies have reported that aqueous GO dispersions generally exhibit strong shear-thinning behavior and concentration-dependent apparent viscosity [45]. These rheological features are highly sensitive to flake size/morphology, oxidation degree, and dispersion stability, and they are commonly used as effective descriptors of GO quality for LbL assembly. Accordingly, the GO used in this study can be considered representative of aqueous GO dispersions widely employed in nanocomposite fabrication. Unless otherwise noted, all solutions were prepared with D.I water (resistivity ≥ 18.2 MΩ cm). For transmission electron microscopy (TEM) analyses, poly (ethylene terephthalate) (PET) film (FilmBank, Gyeonggi-do, Korea) was served as the substrate. Prior to the LbL coating process, PET films were cleaned thoroughly with methanol followed by D.I water, dried using compressed air, and subjected to corona treatment (BD-20C, Chicago, IL, USA) to introduce a negative surface charge. Immediately after treatment, they were dipped sequentially in BPEI and PAA to establish a polyelectrolyte primer layer for subsequent multilayer growth. Silicon (Si) wafers (University Wafer, South Boston, MA, USA) were employed to measure film thickness and investigate surface topography. These substrates were similarly cleaned using a sequence of D.I water, acetone, and D.I water rinses. A quartz crystal microbalance (QCM) (Maxtek, Inc., Cypress, CA, USA) was utilized to investigate the incremental mass gained with each deposition cycle. After each coating step, the crystal was rinsed with D.I water, allowed to air dry, and stabilized to minimize interference from residual water. Flame tests were conducted on 137 μm-thick cotton fabric (areal density 110 $g/m^2$; ISO ADJ Cotton #3262, Test Fabrics, Ansan, South Korea) and flexible PUF (density 0.027 $g/cm^3$; trade name RJBB, JeilDeco Systems, Seoul, South Korea). Both substrates were evaluated under vertical and horizontal flammability conditions to assess the performance of the resultant LbL coatings.

### *2.2. Fabrication of multilayer nanocomposites*

Prior to multilayer deposition, substrates were primed to enhance interfacial adhesion and ensure uniform film growth. Specifically, substrates were first immersed in a BPEI solution (0.1 wt%, pH 10) for 5 min, followed by thorough rinsing with D.I water to remove loosely adsorbed species. Subsequently, the substrates were immersed in a PAA solution (0.2 wt%, pH 4) for 5 min and rinsed again with D.I. water. This primer treatment provided a charged and chemically active surface suitable for subsequent LbL assembly. BL coatings were fabricated by sequentially immersing the primed substrates into BMT and GO dispersions. Each immersion step lasted 5 min during the initial deposition cycle, followed by a 1 min D.I. water rinse between each step to prevent cross-contamination. One complete BMT/GO sequence constituted a single BL. For TL coatings, substrates were sequentially immersed in BMT, PAA, and GO solutions, each for 5 min, with intermediate 1 min D.I. water rinsing steps. One BMT/PAA/GO sequence was defined as one TL. PAA was selected as the interlayer due to its weak polyelectrolyte nature, which enables pH-dependent chain conformation and strong hydrogen-bonding capability under acidic conditions. At low pH, partially protonated PAA effectively bridges BMT and GO through combined hydrogen-bonding and electrostatic interactions, facilitating dense multilayer growth. After the formation of the first BL or TL, the immersion time for subsequent deposition steps was reduced to 1 min per layer, as stable multilayer growth was established. Unless otherwise noted, the pH of all BMT, PAA, and GO coating solutions was adjusted to 2.5 using 0.1 or 1 M HCl. For cotton fabric and PUF samples, an additional pre-treatment step was applied by immersing the samples in a PAA solution (1 wt%, pH 2) for 5 min to introduce a negative surface charge prior to LbL deposition. After each immersion and rinsing step, excess solution was gently removed to ensure uniform deposition and reproducible multilayer growth.

### 2.3. *Characterization*

Film thicknesses of the LbL assemblies were assessed via a NanoMap-PS profilometer (Aeptechnology, Santa Clara, CA, USA). Each reported thickness value reflects at least five measurements across three independent samples (≥15 measurements total). Surface topography was probed by atomic force microscopy (AFM, Nanostation IITM, Herzogenrath, Germany). Morphological features were visualized using field emission scanning electron microscopy (FE-SEM, S-4800, Hitachi, Japan, Core Facility for Supporting Analysis & Imaging of Biomedical Materials at Wonkwang University supported by the National Research Facilities and Equipment Center, NFEC-2008-09-066891). To mitigate charging during SEM analyses, the samples were sputter-coated with a thin layer of platinum (~ 6 nm), and energy-dispersive X-ray spectroscopy (EDX, Oxford Instruments, UK) was performed to determine elemental composition. Cross-sectional micrographs of the LbL coatings were captured using transmission electron microscopy (TEM, JEM-ARM200F, JEOL, Japan). Zeta potential measurements for BMT and GO dispersions were carried out with a Zetasizer Nano ZS90 (Malvern Instruments Ltd., Worcestershire, UK), utilizing a 633-nm laser at a 13° scattering angle. X-ray diffraction (XRD) patterns were obtained using a D/MAX-2500 diffractometer (Rigaku, Japan) equipped with Cu-Kα radiation ($\lambda = 1.541$ Å), to investigate the crystalline organization within the multilayer nanocomposites. Adhesion strength was evaluated using a LUMiFrac® Adhesion Analyzer (LF 200, LUM GmbH, Germany). Adhesion strength was measured using a LUMiFrac® Adhesion Analyzer (LF 200, LUM GmbH, Germany). The specimen was mounted on a rotating rotor and tested at 25 °C with an acceleration rate of 1000 rpm $s^{-1}$ (5 N $s^{-1}$); the critical detachment speed of a circular test stamp (78.54 $mm^2$) supported by a 30 mm × 30 mm wood substrate was recorded to calculate the adhesion strength. Thermogravimetric analyses (TGA) (Q-50, TA Instruments, New Castle, DE, USA) were conducted under nitrogen from ambient temperature to 1000 °C at a 5 °C $min^{-1}$ heating rate to examine the thermal degradation profiles of PUF. TG-IR measurements were performed using a TA Instruments SDT650 coupled with a Nicolet iS50 FT-IR spectrometer (TGA-IR module). Approximately 10-15 mg of sample was heated under $N_2$ from 40 °C to 900 °C at 20 °C $min^{-1}$ with isothermal holds at the beginning (10 min) and end (5 min). To evaluate combustion behavior, both uncoated and coated cotton specimens (9 cm × 30 cm) underwent a bench-scale vertical flame test (ASTM D6413) with a 12 s ignition time, and horizontal flame tests were performed in accordance with ASTM D5132. Cone calorimetry measurements were also carried out under ISO 5660-1 guidelines on 100 mm × 100 mm × 15 mm samples at a heat flux of 35 kW $m^{-2}$ in the horizontal orientation. Finally, as a practical demonstration, the flame resistance of coated PUF was assessed by exposing samples to a direct butane torch flame (Smato, CT-630, Taiwan) for 12 s.

## 3. Results and discussion

### 3.1. *Nanocoating growth behavior*

Two distinct multilayered nanocomposite architectures, BMT/GO BL and BMT/PAA/GO TL systems, were fabricated via an LbL assembly process, as schematically illustrated in Fig. 1a and Fig. S1. The BMT/GO BL system primarily relies on electrostatic attractions between cationic BMT nanoplatelets and anionic GO sheets at pH 2.5. Under these conditions, hydrogen bonding between hydroxyl functionalities on BMT and GO also contributes to film buildup. Partial protonation of the carboxyl groups on PAA and the hydroxyl sites on BMT at pH 2.5 facilitates extensive hydrogen bonding in the BMT/PAA/GO TL, further reinforcing the electrostatic interactions among the three layers (Fig. 1b). Apart from Coulombic forces between oppositely charged species, entropic factors that stem from the release of small counterions serve as an additional thermodynamic driver for LbL film growth [46]. Short-range interactions, such as hydrogen bonding and π–π stacking, could play a significant role in stabilizing the multilayered assemblies [33,47]. Prior to constructing these LbL structures, the colloidal stability of BMT and GO at pH 2.5 was evaluated (Fig. 1c). BMT dispersions remained uniformly suspended, likely due to hydrogen bonding between surface hydroxyl groups and water molecules. Corresponding AFM images of drop-cast BMT confirmed a homogeneous dispersion with minimal aggregation. Similarly, GO exhibited a strong affinity for water, existing in well-exfoliated, two-dimensional nanoplatelets. SEM analyses further corroborated these observations, confirming that both BMT and GO maintain stable, exfoliated nanostructures under the chosen assembly conditions (Fig. S2a and S2b).

The thickness of the LbL coatings on silicon substrates was monitored via stylus profilometry, revealing a linear growth mode for both BL and TL structures (Fig. 2a). The BMT/GO BL system displayed an average thickness increment of approximately 2.4 nm per bilayer. As reported previously, the zeta potential of BMT and GO platelets in the pH range of 2 to 3 is around +27 mV and −25 mV, respectively [48,49]. These values confirm that electrostatic attraction drives the alternating assembly of positively charged clay platelets and negatively charged GO sheets. Incorporating PAA as an intermediate layer in the TL arrangement (BMT/PAA/GO) resulted in a substantially larger growth rate of 27.5 nm per TL, about 11 times greater than that of the BL coatings. This dramatic increase is attributed to the conformational properties of PAA, a weak polyelectrolyte (pKa ~ 5.5-6.5) that undergoes partial protonation at pH 2.5 [50]. Under these conditions, PAA chains exhibit reduced intermolecular repulsion, adopting a more coiled and loop-rich structure [51]. Partially protonated PAA chains adsorb onto BMT surfaces via electrostatic forces at low acidic conditions. In this pH environment, PAA adopts a more coiled form due to reduced repulsion. Since PAA is only partly ionized at pH 2.5, some of its carboxyl groups remain protonated and can form hydrogen bonds with hydroxyl or carboxyl groups on the subsequently deposited GO sheets [52]. In turn, GO layers also engage in ionic and hydrogen-bonding interactions with the next BMT layer, thus continuing the TL assembly process. Through these repetitive LbL cycles, the incorporated PAA chains effectively bridge adjacent BMT and GO layers, filling interstitial gaps and offering additional binding sites for hydrogen bonding and ionic interactions. As a result, more inorganic/organic nanoplatelets are deposited in the TL-based systems, yielding a dramatic increase in thickness.

Fig. 2b presents the results of QCM measurements, which show a nearly linear increase in mass per deposition cycle for BL and TL assemblies, with the TL system exhibiting a higher growth rate. These findings align with profilometry data, indicating that incorporating PAA in each cycle leads to a thicker coating, likely by promoting the deposition of additional BMT and GO-based platelets. The film density, determined by dividing the mass per unit area by the coating thickness, was found to be 1.88 g $cm^{-3}$ for BMT/GO and 2.21 g $cm^{-3}$ for BMT/PAA/GO. The calculated densities of BL and TL multilayer films fall

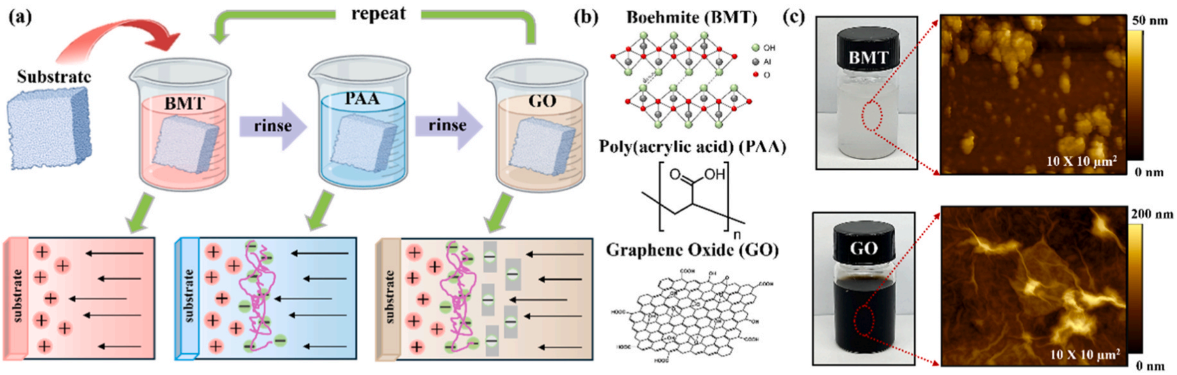

**Fig. 1.** (a) Schematic diagram to assemble BMT/PAA/GO TL nanocomposites, (b) molecular structures of clay, polyelectrolyte, and nanocarbon materials used in this study, and (c) photoimages of vials containing BMT and GO aqueous suspensions. AFM images of the corresponding suspension cast onto Si-wafers are shown next to each of these vials.

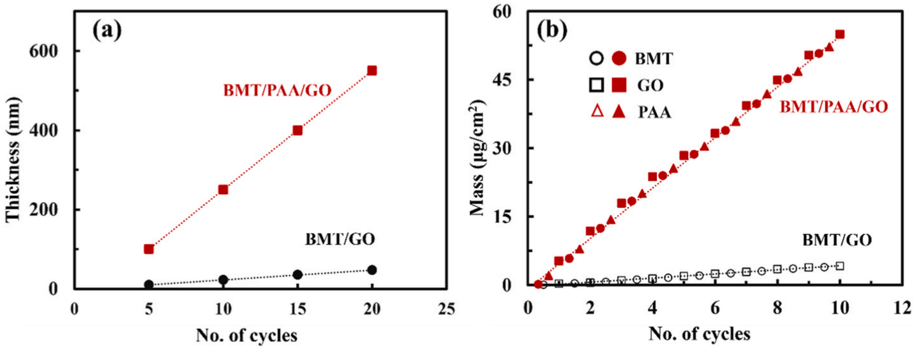

**Fig. 2.** Film thickness as a function of BMT/GO BL and BMT/PAA/GO TL assemblies deposited on Si-wafers.

within the reported range for nanoparticle-based LbL coatings (~1.7-2.4 g cm$^{-3}$) [53,54]. This higher density in the TL systems suggests that a larger amount of clay nanoplatelets and carbon nanomaterials are effectively deposited during each deposition cycle relative to LbL films assembled without polyelectrolytes. The pronounced increase in thickness and mass for the BMT/PAA/GO system compared with BMT/GO

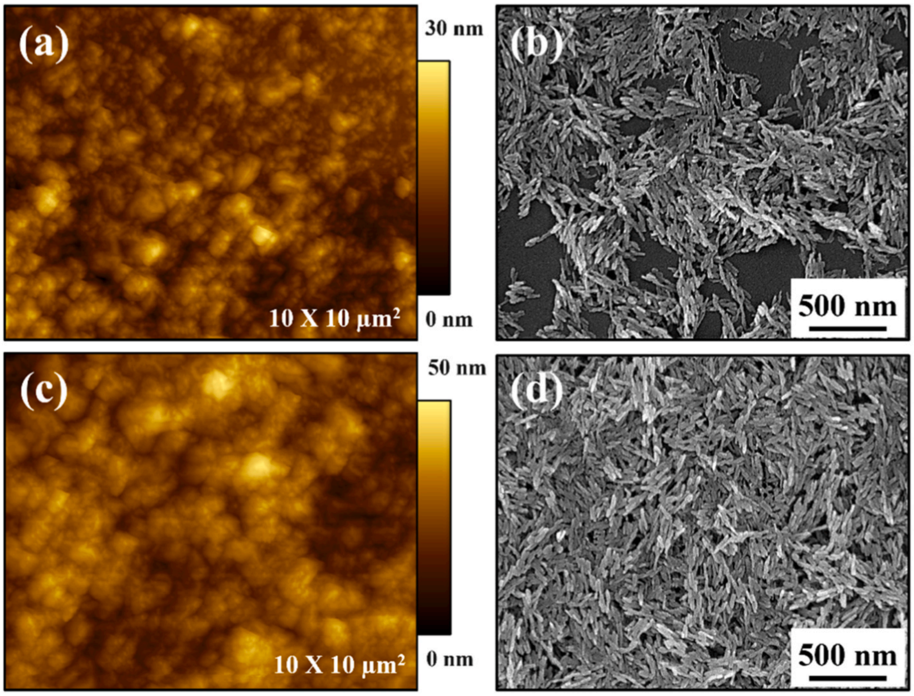

**Fig. 3.** AFM height images of (a) 4 BL BMT/GO and (c) 4 TL BMT/PAA/GO thin films. SEM surface images of (b) 3 BL BMT/GO and (d) 3 TL BMT/PAA/GO nanocomposites.

arises from the role of PAA as a polymeric spacer that strengthens interlayer interactions. PAA, a weak polyanion, is predominantly protonated at pH 2.5, maximizing its hydrogen-bonding capability with BMT/GO. GO exhibits multiple acidic site populations (pKa ~ 3.6, 6.1, 10.1) [55]. Although carboxyl groups on GO are largely protonated at pH 2.5, a non-negligible fraction of oxygen-containing functional groups (e.g., carboxylate and phenolate species) remains partially ionized due to the heterogeneous pKa distribution of GO. These residual ionized sites, which are often concentrated at edge and defect regions, impart a measurable negative surface potential even under acidic conditions, thereby enabling electrostatic pairing with cationic BMT. This dual contribution of hydrogen bonding and electrostatics facilitates denser nanoparticle deposition, yielding thicker and more cohesive coatings, which is expected to promote improved barrier/char formation and is consistent with the enhanced fire performance discussed in the subsequent sections.

### 3.2. *Multilayer structure*

The surface morphology and internal structure of the LbL-assembled nanocomposites were comprehensively investigated through AFM and SEM. AFM images revealed that both BMT platelets and exfoliated GO sheets uniformly covered the surface of the multilayer thin films (Fig. 3a–c and Fig. S3). The TL films displayed a denser arrangement of clay platelets, consistent with the observed increase in film thickness. Correspondingly, SEM micrographs demonstrated a relatively uniform distribution of rod-like BMT particles (150 ~ 200 nm in length) on the film surface, while distinct boundaries of GO nanoplatelets was hardly observed due to its thickness (<2 ~ 3 nm) (Fig. 3b–d and Fig. S4). In line with the AFM findings, TL samples exhibited a more tightly packed surface, featuring closely overlapping BMT and GO platelets with minimal interstitial gaps, compared with BL counterparts. This enhanced packing density suggests that the introduction of PAA interlayer induces stronger electrostatic and hydrogen-bonding interactions, enabling greater incorporation of clay and carbonaceous nanofillers during the assembly process.

TEM images provided a more detailed structure of the LbL coatings coated on PET substrates. As shown in Fig. 4a, BMT nanoparticles were deposited on top of one or two overlapping GO sheets (average lateral dimensions of 1 ~ 1.5 μm), producing a sharp contrast between the denser inorganic platelets and the thinner carbon layers. In top-view TEM images, the TL films appeared more densely covered by both BMT and GO compared to BL structures, in keeping with the increased thickness of the TL coatings (Fig. S5). Cross-sectional TEM micrographs revealed a uniform distribution of BMT and GO throughout the film thickness (Fig. 4b), where distinct, dark lines indicated densely stacked GO layers, while the BMT particles appeared as rod-like or dot-shaped regions. PAA appeared brighter due to much lower electron density. XRD was employed to elucidate the layered arrangement of the LbL-assembled nanocomposites (Fig. 4c). Pristine BMT exhibited characteristic peaks at 2θ ≈ 14.62° and 28.36°, attributed to the (020) and (120) reflections (d-spacings of 0.61 and 0.31 nm, respectively) [56]. Meanwhile, neat GO displayed a (001) reflection at 2θ ≈ 12.88° [57]. In the BL and TL coatings, the GO (001) reflection was not detected, indicating that the LbL process yields exfoliated or turbostratically disordered GO with disrupted long-range registry along the c-axis due to intimate mixing with BMT (and PAA). In the BMT/GO films, the BMT reflections shifted slightly to lower 2θ values (≈14.24° and 28.14°), consistent with a marginal increase in basal spacing (0.62 and 0.32 nm, respectively). In the TL system, these reflections further downshifted to ≈14.1° (d = 0.63 nm) and 27.8° (d = 0.32 nm), suggesting additional gallery expansion associated with the PAA-mediated hybrid assembly. High-magnification cross-sectional TEM images (Fig. 4b and Fig. S6) further corroborate the XRD observations by revealing a disordered, layered hybrid structure in which exfoliated GO sheets are intimately interspersed with BMT platelets rather than forming an ordered, periodically stacked structure. This morphology supports the suppression of GO restacking and indicates a turbostratic hybrid stacking arrangement, consistent with the disappearance of the GO (001) reflection in XRD. In the TL system, the presence of the PAA interlayer facilitates closer interfacial contact and partial intercalation between adjacent inorganic and carbonaceous platelets, leading to a more compact and cohesive multilayer assembly. Such interfacial reorganization results in higher mass loading and packing density, which are directly linked to the formation of a dense and continuous barrier during combustion. Collectively, the combined XRD and TEM analyses demonstrate that the TL coatings exhibit a more integrated hybrid stacking structure than BL films, providing a structural basis for their enhanced thermal shielding and FR performance.

### 3.3. *Thermal stability*

TGA was conducted under nitrogen atmosphere to assess the thermal stability of both uncoated and coated PUF samples (Fig. 5). Uncoated PUF displayed a two-step thermal degradation pathway characteristic of PUF-based materials. The initial degradation, ranging from 220 to 400 °C, corresponds to the breakdown of hard segments and results in the production of primary amines, carbon dioxide, isocyanates, and olefinic compounds [58]. The subsequent decomposition step at around 420 °C, arises from the pyrolysis of the soft segment (polyol) [59]. Beyond 610 °C, the uncoated PUF was essentially fully degraded,

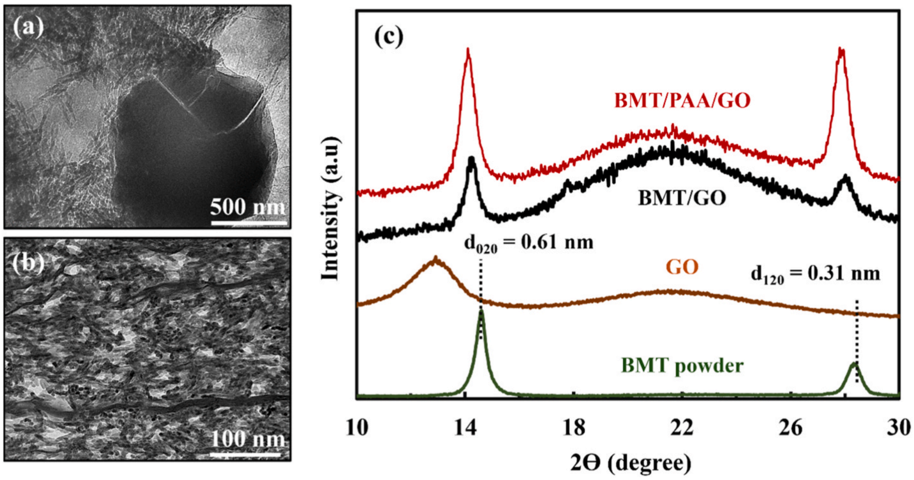

**Fig. 4.** (a) TOP surface and (b) cross-sectional TEM images of BMT/PAA/GO assemblies deposited on PET substrates and (c) XRD patterns for neat BMT (dark green line), GO (brown line), and LbL-assemblies coated with 80 BL BMT/GO (black line) and 20 TL BMT/PAA/GO (red line).

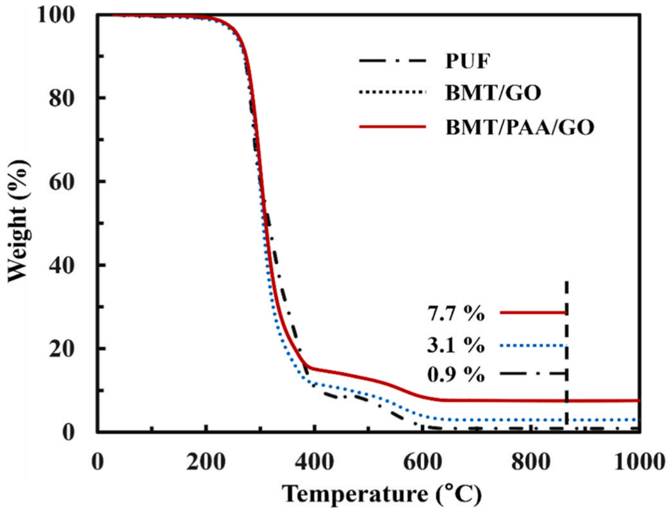

**Fig. 5.** Weight versus temperature for uncoated PUF and 20 BL BMT/GO and 20 TL BMT/PAA/GO LbL assemblies coated on PUF.

leaving only ~ 0.9 wt% of its original mass. In contrast, PUF samples coated with clay/carbon nanoparticle-based LbL assemblies exhibited a comparable thermal degradation profile up to about 430 °C, but generated a higher char residue. This behavior can be attributed to the protective barrier effect imparted by the inorganic clay and carbon constituents. Although both BL and TL-coated foams showed similar overall degradation slopes, the weight-loss rate of the 20 BL BMT/GO-coated foam was greater relative to that of the TL-coated counterparts above 320 °C. Notably, at 860 °C, the char residue for the BL system was 3.1 wt%, whereas the TL coating retained 7.7 wt%, indicating a more substantial deposition of clay and carbon material within the TL nanocomposite. To further elucidate degradation kinetics, DTG (–dW/dT) curves were computed from the TGA traces (Fig. S7). Neat PUF shows a sharp primary DTG maximum characteristic of urethane hard-segment scission, followed by a smaller high-temperature tail from soft-segment pyrolysis. The BL (BMT/GO) retains a similar profile but with a modestly higher peak rate, consistent with nanoparticle-assisted catalysis at early stages. In contrast, the TL (BMT/PAA/GO) displays a reduced peak decomposition rate and a broadened/slightly shifted DTG maximum, indicative of hindered mass transport and stabilized intermediates. These kinetic signatures correlate with the greater char residue of TL at high temperature and the more continuous surface char observed after cone tests, supporting the role of the PAA interlayer in densifying the multilayer and reinforcing the protective carbon/ceramic barrier. Although PAA itself is less thermally stable than inorganic BMT or carbonaceous GO, its role as a bridging interlayer enhances multilayer buildup by promoting hydrogen bonding and electrostatic interactions. As confirmed by thickness, QCM, and microscopy data, the TL coatings incorporate greater amounts of BMT and GO than BL counterparts. The predominance of these inorganic and carbonaceous constituents explains the higher residual char observed for TL coatings. Such enhanced char formation contributes directly to the improved flame retardancy observed during combustion testing.

To directly verify the mechanism of char enhancement, we performed Raman spectroscopy on the residues. Raman spectra of the BL and TL assemblies before and after flame exposure are presented in Fig. S8. Both systems showed distinct D (~1360 $cm^{-1}$) and G (~1588 $cm^{-1}$) bands. Prior to combustion, their $I_D/I_G$ ratios were nearly identical, reflecting similar structural disorder. Following flame tests, the BL system showed only a moderate decrease in $I_D/I_G$, while the TL system exhibited a more significant reduction. The larger decrease in $I_D/I_G$ for the TL coatings indicates that PAA facilitates enhanced graphitization upon burning, producing a more ordered char structure. This improved carbonaceous char accounts for the superior flame retardant efficiency of the TL assemblies compared with BL. XPS analyses of the BMT/GO and BMT/PAA/GO coatings further revealed that PAA strengthens interfacial chemistry prior to burning and promotes the formation of a more graphitized/ceramic char after burning (Fig. S9). In the C 1s spectra, the TL displayed stronger oxygenated components (C–O at ~286.9 eV; O–C=O at ~288.5–289 eV) relative to the BL, as expected for PAA/GO-containing films. After burning, the C 1s peak in both systems shifted toward $sp^2$ C–C with diminished oxygenated carbons, evidencing graphitization; this effect was more pronounced for TL. In the Al 2p spectra, both systems retained an Al–O signal with a peak near 74.9 eV; however, the TL exhibited a slight negative chemical shift (~74.4 eV) compared with BL, consistent with carboxylate coordination/screening and BMT dehydroxylation toward $\gamma$-$Al_2O_3$ during burning. These results confirm that PAA mediated interfacial bonding to BMT before burning and yielded a more graphitized carbon matrix anchored to an alumina-rich ceramic skeleton after burning, thereby explaining the larger char amount and superior flame-retardant performance of TL compared with BL.

### 3.4. Mechanical behaviors

To evaluate mechanical integrity on compliant substrates, we measured compressive stress-strain responses of PUF coated with 10 BL BMT/GO and 10 TL BMT/PAA/GO, and compared them to uncoated PUF (Fig. 6a). Under quasi-static compression to ~70% strain, both coatings increased the stress across the plateau and densification regimes. At approximately 7% strain, the compressive stress was about 0.009 MPa for the uncoated foam, increased to roughly 0.014 MPa for the 10-BL coating, and reached around 0.015 MPa for the 10-TL coating. When the strain was extended to 70%, the stresses rose to ~0.015 MPa for the uncoated foam, ~0.019 MPa for the 10-BL sample, and 0.023 MPa for the 10-TL sample. Thus, the TL coating raises the apparent compressive stress by ~ 50% at 70% strain relative to the uncoated foam (BL: ~20% at 70%), which is consistent with the formation of denser and more cohesive multilayers afforded by the PAA interlayer. These results, together with the water-immersion FR retention and compression-set data, demonstrate that the multilayer coatings remain adherent on compliant PUF and mechanically reinforce the foam under compressive loading.

The centrifugal adhesion test results demonstrated that the multilayer nanocoatings significantly enhance the structural integrity of the control samples (Fig. 6b). The uncoated PUF exhibited a baseline adhesion stress of only 0.41 MPa, indicating weak interfacial bonding between the foam surface and the test stamp. However, this value increased to 2.51 MPa with the BMT/GO BL coating, demonstrating improved interfacial cohesion due to the inorganic nanoplatelet network. Notably, the BMT/PAA/GO TL system achieved the highest adhesion strength of 3.89 MPa, reflecting the role of the PAA interlayer in promoting stronger interfacial interactions and cohesive multilayer formation. These results confirm that the polymer-assisted LbL architecture substantially improves coating robustness and interfacial durability on compliant PUF substrates. Representative studies on polymer-clay nanocomposite coatings have emphasized the importance of mechanical robustness for long-term protective performance [60]. In this context, the improved adhesion and washing durability observed in the present TL system further support the practical stability of the interlayer-mediated LbL architecture. The compressive set tests (77 °C, 22 h, 51% compression) revealed that the uncoated PUF retained excellent elasticity (2.6%), whereas the BMT/PAA/GO-coated foams (10 TL) exhibited a higher compression set of 32.6%. Although the TL-coated foams exhibit an increased compression set due to the presence of rigid inorganic/graphenic layers, such values remain acceptable for FR applications where fire safety and structural integrity are prioritized over maximal elastic recovery.

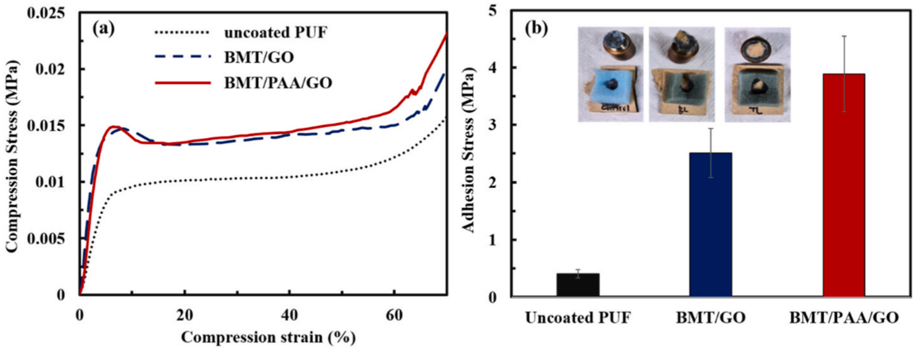

**Fig. 6.** (a) Compressive stress-strain curves of uncoated PUF, 10 BL BMT/GO, and 10 TL BMT/PAA/GO PUF under compression up to ~70% strain. (b) Adhesion strength of uncoated and LbL-coated polyurethane foam (PUF) measured using a centrifugal adhesion test. Inset: Photographs of the adhesion test stamps after centrifugal detachment, showing the failure mode and residual coating on uncoated and LbL-coated PUF samples.

### *3.5. Flame retardant properties of multilayer nanocomposites*

### *3.5.1. Flame-retardant performance of LbL-Coated cotton fabrics*

To evaluate the FR performance of the LbL-based coatings, VFT was conducted under standardized conditions. The mass gain (add-on) associated with the coated fabrics was quantified by weighing the samples before and after the deposition of the nanostructured layers, confirming a linear increase in coating add-on with the number of deposited layers (Table S1, Supporting Information). The TRL systems exhibited a higher overall mass uptake compared to that of BL counterparts. During VFT, uncoated fabrics ignited rapidly and were almost entirely consumed with minimal char formation (Fig. 7, middle row). In contrast, fabrics with no polymers deposited left significant residues. With the addition of the polymers in between BMT and GO layers, the residual char of fabrics after flame was increased, indicating that the introduction of PAA in the multilayers improves the fire resistance and provides more effective FR behaviors.

SEM was employed to elucidate morphological variations in the FR nanocoating before and after VFT. Prior to flame exposure, the uncoated fabric exhibited a relatively smooth surface (Fig. 7, top). In contrast, SEM images of the BMT/GO-coated fabrics clearly showed that each fiber was conformally coated, indicating successful LbL deposition. At higher magnification, the PAA-containing TL systems displayed a rougher surface topology and more aggregates on the fiber surfaces. Post-combustion micrographs for the uncoated control were not available, as the fabric was fully consumed by the flame. Both BL- and TL-coated samples retained their macroscopic weave structure and fiber architecture following VFT (Fig. 7, bottom). Subsequent high-resolution SEM observations (Fig. S10, Supporting Information) revealed that the clay platelets and GO nanoparticles remained adhered to individual

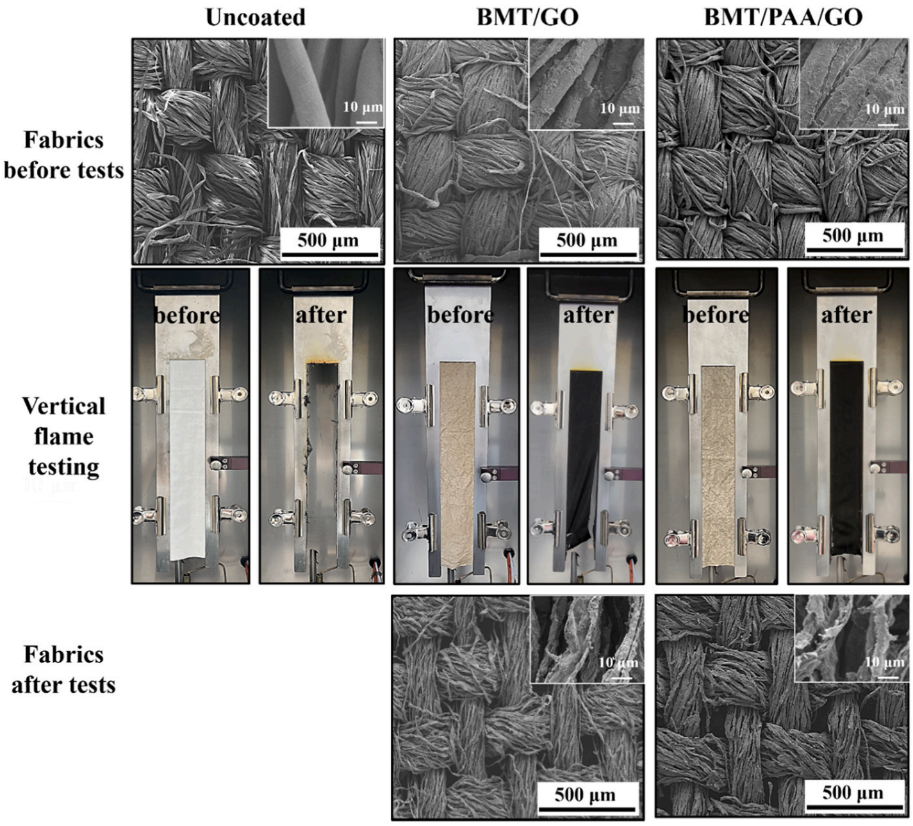

**Fig. 7.** SEM images of fabrics before (top) and after (bottom) vertical flame tests and photographs (middle) taken before and after vertical flame tests of uncoated and 10 BL BMT/GO and 10 TL BMT/PAA/GO-coated fabrics.

fibers. These inorganic platelets and carbon materials appeared partially coalesced after exposure to high temperatures, thereby producing a relatively smooth yet robust char layer on the fiber surfaces. HFT testing was performed on the same coated textiles to further investigate flammability characteristics of multilayer nanocomposites. While the uncoated fabric was entirely consumed with negligible char residue, all LbL-coated samples generated substantial residual mass (Fig. S11, Supporting Information), confirming the improved FR performances of the nanostructured coatings. To further validate the synergistic effect of the BMT/PAA/GO TL system, cotton fabrics were immersed separately in BMT, GO, or PAA aqueous dispersions for 10 min to generate single-component coatings. After drying, the samples were subjected to vertical flame testing under identical conditions. As shown in Fig. S12, the fabrics coated with only BMT, GO, or PAA were almost completely consumed by the flame, leaving negligible residue. These results confirm that the observed FR performance cannot be ascribed to additive effects of single components alone but rather originates from the synergistic interaction among BMT, GO, and/or PAA layers in the LbL configuration.

To examine the water stability of the BMT/GO and BMT/PAA/GO assemblies, we immersed the coated fabrics (10 layers) in D.I water for 24 h. After drying under ambient conditions, the samples were subjected to vertical flame tests. As shown in Fig. S13, both BL and TL systems retained their FR performance after immersion. The photographs taken before and after the flame test clearly demonstrated that the coatings did not delaminate from the fabric substrates and continued to provide effective protection, as evidenced by the self-extinguishing behavior and the intact structure of the char residues. Wash durability was evaluated according to AATCC 135 by laundering the coated fabrics with detergent. The 10 TL BMT/PAA/GO-coated cotton fabrics maintained their structural integrity after five home laundering cycles, as shown in Fig. S14. Subsequent horizontal flame tests revealed that the washed TL samples still exhibited effective FR behavior, leaving substantial char residue and preserving the fibrous architecture, whereas insufficiently stabilized coatings would typically deteriorate after repeated washing. These results indicate that the interlayer-mediated TL architecture provides strong interfacial cohesion, arising from cooperative interactions among BMT, PAA, and GO, thereby enhancing coating stability during laundering while retaining FR performance.

### *3.5.2. Flame-retardant performance of LbL-Coated polyurethane foam*

Cone calorimetry was employed to quantitatively characterize the intrinsic thermal barrier performance of the LbL nanocoatings applied to PUF. Under an external heat flux of 35 kW$^{-2}$, the heat release rate (HRR), a key indicator of fire risk, was monitored over time (Fig. 8). The uncoated PUF exhibited two pronounced HRR peaks, consistent with the multi-stage pyrolysis and combustion behavior typical of PUF-based materials [61,62]. The first HRR peak (pkHRR) reached approximately 247.3 kW m$^{-2}$ within 14 s of ignition, concomitant with foam collapse. Subsequent melting facilitated more rapid volatilization of decomposition products, reaching in a higher secondary peak (451.9 kW m$^{-2}$) after 28 s. PUF coated with 10 BL of BMT/GO (~25 nm thickness) demonstrated analogous HRR profiles to the neat control; however, the second peak HRR dropped to 174.2 kW m$^{-2}$, corresponding to a 61.5% reduction compared with the uncoated foam. Interestingly, the first HRR peak for the coated foam (344.1 kW m$^{-2}$) was larger that of the neat PUF. The observed increase in the initial peak heat release rate is attributed to the catalytic effect of nanoparticles within the coating and the initial combustion of the polyelectrolytes (*i.e.*, BPEI and PAA as an LbL coating primer) [63,64]. This phenomenon can be interpreted as a competitive mechanism in which early-stage catalysis and polyelectrolyte decomposition accelerate the establishment of a stable char layer. Consequently, this robust char barrier effectively suppresses the second, more hazardous heat release rate peak, thereby significantly reducing the overall fire risk. To investigate the potential for premature catalytic degradation, TG-IR analysis was conducted (Fig. S15), revealing that the intrinsic pyrolysis pathways of the PUF remained completely unaltered by the LbL nanocoatings. Across all uncoated and coated samples, identical volatile species were detected: isocyanic acid and tolylene 2, 4-diisocyanate during the first degradation stage (~15.2 min), followed by polyether/polyol derivatives, $CO_2$, and $H_2O$ during the second stage (~19.4 min). This consistency in the evolved gas profiles confirms that the early-stage HRR increase is not driven by chemically catalyzed pyrolysis, but rather by the delayed formation of a continuous physical barrier prior to robust char accumulation. The slightly elevated HRR observed in longer time regimes for clay-based nanocomposite coatings can be explained by their inherent thermal insulation and char-forming effects. These coatings reduce heat transfer to the substrate, delaying polymer degradation and resulting in a sustained HRR profile over time. In addition, the protective clay-carbonaceous char formed on the surface acts as an insulating barrier, but its development involves gradual volatile release through the evolving char structure. This combination of delayed degradation and controlled combustion accounts for the higher HRR at later stages, while still eliminating the hazardous secondary peak and improving overall fire resistance.

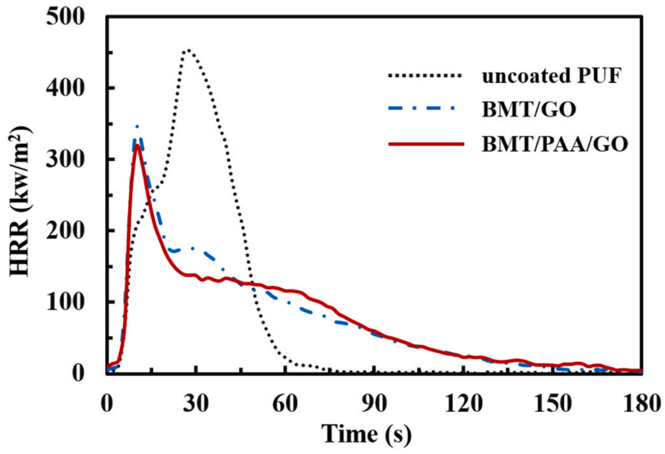

**Fig. 8.** Heat-release rate (HRR), as a function of time, during cone calorimeter testing, for uncoated control and 10 BL BMT/GO and 10 TL BMT/PAA/GO assemblies that are coated on PUF.

The application of 10 TL BMT/PAA/GO coating, which is ~ 250 nm thick, substantially enhanced the FR performance of PUF. Compared with BL assemblies of similar composition, the TL system lowered the first peak of HRR by about 7.5% and effectively eliminated the second HRR peak. In addition to HRR, cone calorimetry parameters such as total smoke release (TSR), total smoke production (TSP), maximum average rate of heat emission (MARHE), and effective heat of combustion (EHC) were obtained for each sample (Table 1 and Fig. S16). Each reported value was obtained as the average of three independent cone calorimeter tests for each sample. Compared with uncoated PUF, the TL coatings reduced TSR, TSP, MARHE, and EHC by 58.7%, 60.0%, 42.9%, and 11.3%, respectively, whereas the BL coatings achieved smaller decreases of 38.9%, 53.8%, 15.6%, and 4.6%. Although the improvement in EHC between TL and BL systems is modest, the overall suppression of smoke

**Table 1**

Cone calorimeter results for polyurethane foam with and without nanocoatings. TSR, TSP, MARHE, and EHC stand for total smoke release, total smoke production, maximum average rate of heat emission, and effective heat of combustion, respectively.

| Sample | TSR ($m^2/m^2$) | TSP ($m^2$) | MARHE (kW/$m^2$) | EHC (MJ/kg) |
|---|---|---|---|---|
| **Control** | **175.2 ± 10.1** | **1.5 ± 0.2** | **285.1 ± 14.2** | **30.2 ± 1.8** |
| **BMT/GO** | **118.5 ± 7.5** | **1.3 ± 0.1** | **192.6 ± 9.5** | **28.1 ± 1.3** |
| **BMT/PAA/GO** | **72.4 ± 6.7** | **0.6 ± 0.1** | **162.6 ± 8.3** | **26.8 ± 1.1** |

release and heat emission is significantly greater in the TL system, confirming that the incorporation of PAA layers enhances the fire performance of the hybrid nanocoatings. Post-burn images revealed that TL-coated foams largely retained their original structure and produced a durable char residue, whereas both the neat foam and BL-coated samples were almost completely consumed (Fig. S17). Over extended burn periods, the LbL-coated samples exhibited a rise in HRR, which is presumably attributed to the heat-shielding characteristics of the organic–inorganic hybrid layers. These nanocomposite coatings effectively slow heat transfer from the flame, resulting in a delayed ignition phase; however, once combustion processes become established, an elevated HRR may emerge. Simultaneously, the nanocomposite structure promotes the formation of a charred protective barrier on the surface. While this char layer insulates the underlying substrate against thermal damage, its gradual development can retain pyrolysis products and thermal energy, potentially leading to an increase in HRR as trapped volatiles are released and combusted over time. Although the FR action is primarily governed by condensed-phase mechanisms, some secondary gas-phase contributions cannot be excluded. BMT releases $H_2O$ during dehydroxylation, while decomposition of the primer layers (BPEI and PAA) may generate $N_2$, $NH_3$, and $CO_2$, which can dilute flammable volatiles and contribute modestly to flame suppression. Conventional FR systems such as ammonium polyphosphate, aluminum trihydroxide, and phosphorus compounds typically require high loadings (>20-40 wt%) to realize significant reductions in fire parameters, which can adversely affect mechanical integrity. In comparison, the present BMT/PAA/GO hybrid system effectively achieves a marked reduction in HRR and THR at significantly lower additive levels (<10 wt%). This highlights the advantage of nanostructured hybrid FR as competitive alternatives to standard commercial additives.

A 12-sec torch-flame test was conducted to quantitatively evaluate the FR performance of the coated PUF. Under direct flame exposure, the neat PUF rapidly melted, generating dense smoke and pronounced melt dripping, which is behavior indicative of its limited thermal stability and propensity for secondary fire damage (Video S1). In contrast, PUF coated with BMT/GO exhibited substantially reduced dripping, though its foam matrix underwent significant collapse once the flame had traversed the surface, leaving a residual mass of only ~20 wt% (Fig. S18 and Video S2). Incorporating additional polymer layers into the BL-based nanocoating enhanced the FR properties of the foam. BMT/PAA/GO LbL coatings displayed only partial decomposition with negligible dripping, thus preserving the foam's macroscopic structure during torch testing (Video S3). Cross-sectional analysis of the TL-coated PUF confirmed that the underlying foam, beneath the protective char layer, remained largely intact, retaining ~85 wt% of its original mass. These observations demonstrate the superior barrier performance of the TL coating, attributable to both its increased thickness and its higher loading of carbonaceous and clay components compared to BL systems.

Supplementary data related to this article can be found online at.

Fig. 9a, b and Fig. S19 present photographic and SEM images of the uncoated PUF, highlighting its characteristic three-dimensional, open-pore morphology and relatively smooth cell walls. PUF treated with the TL system also retained its native porosity and cell size, and exhibited a uniformly deposited nanolayer across the open-cell framework (Fig. 9d

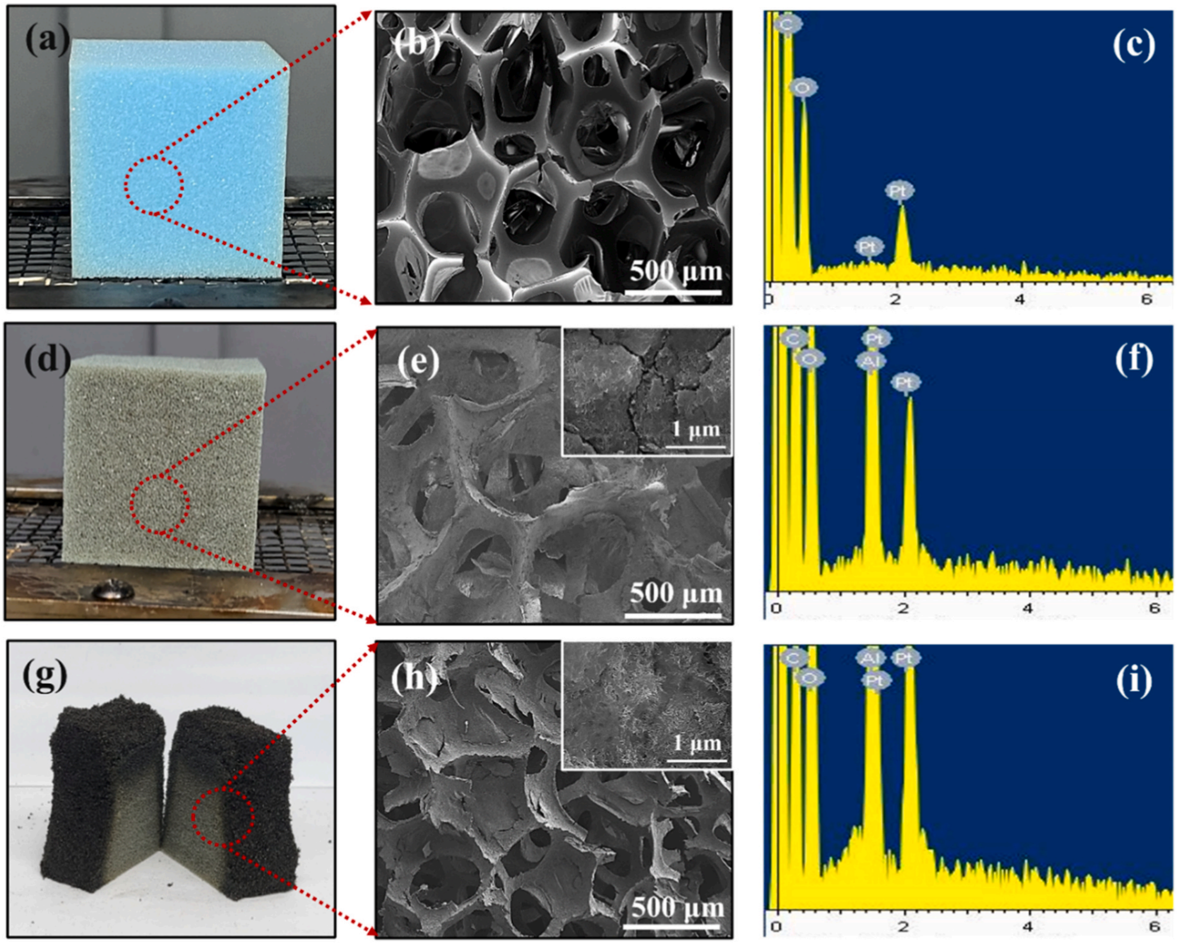

**Fig. 9.** Photo images ((a), (d), and (g)) (left column), SEM images ((b), (e), and (h)) (middle column), and corresponding EDX analyses ((c), (f), and (i)) (right column) showing neat PUF and 10 TL BMT/PAA/GO-coated PUF before and after torch tests. The inset images at high magnification show carbonaceous materials/clays-based structure deposited on the foam surface.

and e). Higher-magnification views confirmed the conformal coverage of clay/graphene oxide (GO) platelets achieved through the LbL process (inset in Fig. 9e). At the boundary between the black charred region and the underlying foam (Fig. 9g and h), the foam's core shape was preserved after a torch burn test, with higher-magnification images revealing that the residual char consisted primarily of aggregated clay/GO structures (inset in Fig. 9h). Post-combustion residues of the TL-coated PUF were further investigated via EDX spectroscopy (Fig. 9, right column), confirming that the elemental composition of the BMT/PAA/GO coating remained essentially unchanged before and after flame exposure. These observations demonstrated the robust flame resistance and structural stability offered by the FR coating, protecting both the chemical integrity and the mechanical framework of the PUF under high-temperature conditions. Post-burn SEM and EDX analyses showed adherent, reinforced chars maintaining contact with the substrate, with no visible large-area delamination despite thermal exposure. Together with the moderate film thickness (∼250 nm), these observations suggest that the present TL architecture mitigates crack or delamination issues commonly reported for thicker, highly inorganic LbL coatings. A comparative overview of representative state-of-the-art LbL FR systems is provided in Table S2. Beyond ultrathin LbL architectures, the synergistic FR effects of multidimensional nanomaterials (e.g., GO, clays, and functionalized metal oxides) have also been successfully translated into broader materials design contexts. For instance, incorporating these nanofillers into bulk polymer matrices or as thick hybrid protective coatings on rigid substrates has demonstrated exceptional capabilities in significantly suppressing pHRR and providing multi-functional barrier protection in advanced industrial applications [65,66].

This work demonstrates a highly efficient FR system in which organic/inorganic nanoplatelets form a well-ordered multilayer structure through relatively few deposition steps. Analyses using TGA, VFT/HFT, and cone calorimetry revealed that BMT and GO act synergistically to improve the fire resistance of cotton fabrics and PUF. The enhanced flame retardancy of the BMT/PAA/GO TL coatings arises from multiple synergistic mechanisms [67–69]. BMT acts as a ceramic-like barrier that resists thermal degradation and releases bound water during dehydroxylation, thereby diluting flammable volatiles and lowering flame temperature. GO, with its layered topology and high thermal stability, contributes to the formation of compact graphitic char that restricts heat and mass transfer while reinforcing the protective layer. Beyond these inorganic and carbonaceous contributions, the incorporation of PAA as an interlayer further enhances performance by increasing nanoparticle deposition per cycle. At pH 2.5, PAA promotes stronger electrostatic attraction and hydrogen bonding between oppositely charged species, which facilitates denser and more cohesive multilayer growth. Moreover, the functional groups of GO improve adhesion with both BMT and PAA, ensuring uniform coverage and filling of interstitial gaps. This polymer-assisted architecture produces highly aligned and compact nanoplatelet assemblies that yield robust, carbonaceous–ceramic char residues during combustion. Collectively, these complementary effects explain the significant reductions in pkHRR, TSR, and TSP observed for the TL system, confirming that the PAA-mediated hybrid design promotes a synergistic, multi-pathway FR response. Such findings reveal the importance of polymeric interlayers in advancing the protective function of clay/GO coatings, thereby offering an effective and eco-friendly strategy to impart superior flame resistance to textile and foam substrates.

## 4. Conclusion

In conclusion, this study demonstrates that water-based, halogen-free coatings composed of BMT, PAA, and GO, integrated via LbL assembly, substantially improve the fire resistance of cotton fabrics and PUF. The incorporation of a PAA interlayer between BMT and GO produced TL systems with significantly increased thickness and mass deposition compared to simple bilayer BL coatings. Assembled under acidic conditions (pH ∼2.5), the partially protonated PAA enables a cooperative interplay of chain mobility, electrostatic attraction, and hydrogen-bonding. Crucially, the PAA interlayer does not merely increase material deposition but exerts a distinct synergistic effect. By densifying the hybrid architecture, as confirmed by XRD and TEM characterizations, this highly cohesive structure actively regulates the charring chemistry. It promotes enhanced graphitization and yields a robust carbonaceous-ceramic barrier that far surpasses simple additive mass effects. Consequently, vertical and horizontal flame tests confirmed that coated fabrics maintained their structural integrity and produced substantial char residue, whereas uncoated controls were completely consumed. For PUF, cone calorimetry revealed that while 10 BL coatings suppressed the second peak heat release rate (pkHRR) by over 60%, the corresponding TL systems fully eliminated the second pkHRR and concurrently reduced TSR, TSP, MARHE, and EHC. Despite these promising results, conventional LbL methods remain constrained by sequential dipping steps and extended drying times. Future work should explore accelerated and scalable approaches, such as spray-assisted LbL, roll-to-roll deposition, or automated dipping platforms, to overcome these limitations and enable the practical deployment of multifunctional FR coatings across diverse industrial applications.

## CRediT authorship contribution statement

**Inyoung Lee:** Investigation, Data curation, Conceptualization. **Yong Chae Jung:** Investigation, Resources, Validation. **Yong Tae Park:** Writing – original draft, Investigation, Data curation. **Jung Sang Cho:** Writing – original draft, Investigation, Conceptualization. **Chungyeon Cho:** Writing – review & editing, Writing – original draft, Methodology, Investigation, Data curation, Conceptualization.

## Declaration of competing interest

The authors declare that they have no known competing financial interests or personal relationships that could have appeared to influence the work reported in this paper.

## Acknowledgements

This work was supported by the National Research Foundation of Korea (NRF) grant funded by the Korea government (MSIT) (No. RS-2024-00405537). This research was also supported by the Institute of Information & Communications Technology Planning & Evaluation (IITP)-Innovative Human Resource Development for Local Intellectualization program grant funded by the Korea government (MSIT) (IITP-2026-RS-2024-00439292).

## Appendix A. Supplementary data

Supplementary data to this article can be found online at https://doi.org/10.1016/j.mtchem.2026.103531.

## Data availability

No data was used for the research described in the article.

## References

[1] Z. Qiang, H. Wenjun, W. Yanbin, L. Xingjian, Z. Yiheng, Functionalization of polyurethane based on copper-catalyzed azide-alkyne cycloaddition reaction, Prog. Chem. 32 (2020) 147.

[2] H.W. Engels, H.G. Pirkl, R. Albers, R.W. Albach, J. Krause, A. Hoffmann, H. Casselmann, J. Dormish, Polyurethanes: versatile materials and sustainable problem solvers for today's challenges, Angew. Chem. 52 (2013) 9422–9441.

[3] J.O. Akindoyo, M. Beg, S. Ghazali, M. Islam, N. Jeyaratnam, A. Yuvaraj, Polyurethane types, synthesis and applications–A review, RSC Adv. 6 (2016) 114453–114482.

[4] W.-W. Gao, G.-X. Zhang, F.-X. Zhang, Enhancement of flame retardancy of cotton fabrics by grafting a novel organic phosphorous-based flame retardant, Cellulose 22 (2015) 2787–2796.

[5] S. Shaw, Halogenated flame retardants: do the fire safety benefits justify the risks? Reveh 25 (2010) 261–306.

[6] S. Bocchini, G. Camino, Halogen-containing flame retardants, Fire Retar. Polym. Mater. 2 (2010) 75–106.

[7] M. Altarawneh, A. Saeed, M. Al-Harahsheh, B.Z. Dlugogorski, Thermal decomposition of brominated flame retardants (BFRs): products and mechanisms, PECS 70 (2019) 212–259.

[8] M. Liu, J. Qiao, X. Zhang, Z. Guo, X. Liu, F. Lin, M. Yang, J. Fan, X. Wu, Z. Huang, Flame retardant strategies and applications of organic phase change materials: a review, Adv. Funct. Mater. 35 (2025) 2412492.

[9] X. Wang, W. Guo, W. Cai, J. Wang, L. Song, Y. Hu, Recent advances in construction of hybrid nano-structures for flame retardant polymers application, Appl. Mater. Today 20 (2020) 100762.

[10] X. Li, C. Liu, X y An, L. Niu, J. Feng, Z m Liu, Construction and mechanism of efficient flame retardant system for alkali lignin-enhanced rigid polyurethane foam, J. Appl. Polym. Sci. 141 (2024) e55827.

[11] A. Kausar, A review of high performance polymer nanocomposites for packaging applications in electronics and food industries, J. Plast. Film Sheeting 36 (2020) 94–112.

[12] S. Sharma, A. Verma, S.M. Rangappa, S. Siengchin, S. Ogata, Recent progressive developments in conductive-fillers based polymer nanocomposites (CFPNC's) and conducting polymeric nanocomposites (CPNC's) for multifaceted sensing applications, J. Mater. Res. Technol. 26 (2023) 5921.

[13] M.M. Shameem, S. Sasikanth, R. Annamalai, R.G. Raman, A brief review on polymer nanocomposites and its applications, Mater. Today 45 (2021) 2536–2539.

[14] T. Sai, S. Ran, Z. Guo, P. Song, Z. Fang, Recent advances in fire-retardant carbon-based polymeric nanocomposites through fighting free radicals, SusMat 2 (2022) 411–434.

[15] I. Lee, J. Kim, S. Yun, J. Jang, S.Y. Cho, J.S. Cho, J.H. Ryu, D. Choi, C. Cho, Synergistic combination of dual clays in multilayered nanocomposites for enhanced flame retardant properties, ACS Omega 9 (2024) 6606–6615.

[16] M.S. Murad, A.K. Hamzat, E. Asmatulu, R. Asmatulu, Flame-retardant fiber composites: synergistic effects of additives on mechanical, thermal, chemical, and structural properties, Adv. Compos. Hybrid Mater. 8 (2025) 1–43.

[17] W. Zhan, L. Chen, F. Cui, Z. Gu, J. Jiang, Effects of carbon materials on fire protection and smoke suppression of waterborne intumescent coating, Prog. Org. Coating 140 (2020) 105491.

[18] L.T. Temane, S.S. Ray, J.T. Orasugh, Review on processing, flame-retardant properties, and applications of polyethylene composites with graphene-based nanomaterials, Macromol. Mater. Eng. (2024) 2400104.

[19] W. He, P. Song, B. Yu, Z. Fang, H. Wang, Flame retardant polymeric nanocomposites through the combination of nanomaterials and conventional flame retardants, Prog. Mater. Sci. 114 (2020) 100687.

[20] Y. Lee, C.B. Park, M. Sain, M. Kontopoulou, W. Zheng, Effects of clay dispersion and content on the rheological, mechanical properties, and flame retardance of HDPE/clay nanocomposites, J. Appl. Polym. Sci. 105 (2007) 1993–1999.

[21] Wilkie C A, Horrocks A R, Hornsby P, Flame retardant fillers, Fire Retardancy of Polymeric Materials, CRC Press, pp. 97-115.

[22] J. Kim, J. Jang, S. Yun, H.D. Kim, Y.Y. Byun, Y.T. Park, J.I. Song, C. Cho, Synergistic flame retardant effects of carbon nanotube-based multilayer nanocoatings, Macromol. Mater. Eng. 306 (2021) 2100233.

[23] B.W. Liu, H.B. Zhao, Y.Z. Wang, Advanced flame-retardant methods for polymeric materials, Adv. Mater. 34 (2022) 2107905.

[24] S. Araby, B. Philips, Q. Meng, J. Ma, T. Laoui, C.H. Wang, Recent advances in carbon-based nanomaterials for flame retardant polymers and composites, Compos. B Eng. 212 (2021) 108675.

[25] A. Kausar, Z. Anwar, B. Muhammad, Overview of nonflammability characteristics of graphene and graphene oxide-based polymeric composite and essential flame retardancy techniques, Polym-Plast. Technol. 56 (2017) 488–505.

[26] C.-F. Cao, B. Yu, Z.-Y. Chen, Y.-X. Qu, Y.-T. Li, Y.-Q. Shi, Z.-W. Ma, F.-N. Sun, Q.-H. Pan, L.-C. Tang, Fire intumescent, high-temperature resistant, mechanically flexible graphene oxide network for exceptional fire shielding and ultra-fast fire warning, Nano-Micro Lett. 14 (2022) 92.

[27] L. Zuo, W. Fan, Y. Zhang, L. Zhang, W. Gao, Y. Huang, T. Liu, Graphene/montmorillonite hybrid synergistically reinforced polyimide composite aerogels with enhanced flame-retardant performance, Compos. Sci. Technol. 139 (2017) 57–63.

[28] O.M. Sanusi, A. Benelfellah, N.A. Hocine, Clays and carbon nanotubes as hybrid nanofillers in thermoplastic-based nanocomposites–A review, Appl. Clay Sci. 185 (2020) 105408.

[29] R D Maalihan, M R B Domalanta, A C C Corrales, E B Caldona, Advances in interfacially engineered surface-functionalized fillers for multifunctional polymer composite coatings, Polym. Compos.46 (2025) 5857.

[30] X. Zhang, Y. Xu, X. Zhang, H. Wu, J. Shen, R. Chen, Y. Xiong, J. Li, S. Guo, Progress on the layer-by-layer assembly of multilayered polymer composites: strategy, structural control and applications, Prog. Polym. Sci. 89 (2019) 76–107.

[31] W. Yuan, G.-M. Weng, J. Lipton, C.M. Li, P.R. Van Tassel, A.D. Taylor, Weak polyelectrolyte-based multilayers via layer-by-layer assembly: approaches, properties, and applications, Adv. Colloid Interface Sci. 282 (2020) 102200.

[32] M. Keeney, X. Jiang, M. Yamane, M. Lee, S. Goodman, F. Yang, Nanocoating for biomolecule delivery using layer-by-layer self-assembly, J. Mater. Chem. B 3 (2015) 8757–8770.

[33] Z. Zhang, J. Zeng, J. Groll, M. Matsusaki, Layer-by-layer assembly methods and their biomedical applications, Biomater. Sci. 10 (2022) 4077–4094.

[34] J. Borges, J. Zeng, X.Q. Liu, H. Chang, C. Monge, C. Garot, K f Ren, P. Machillot, N. E. Vrana, P. Lavalle, Recent developments in layer-by-layer assembly for drug delivery and tissue engineering applications, Adv. Healthcare Mater. 13 (2024) 2302713.

[35] P.T. Hammond, Engineering materials layer-by-layer: challenges and opportunities in multilayer assembly, AIChE J. 57 (2011) 2928–2940.

[36] X.-H. Shi, Y.-J. Xu, J.-W. Long, Q. Zhao, X.-M. Ding, L. Chen, Y.-Z. Wang, Layer-by-layer assembled flame-retardant architecture toward high-performance carbon fiber composite, Chem. Eng. J. 353 (2018) 550–558.

[37] X. Qiu, Z. Li, X. Li, Z. Zhang, Flame retardant coatings prepared using layer by layer assembly: a review, Chem. Eng. J. 334 (2018) 108–122.

[38] A. Priyadharshini, J.R. Xavier, A review on functional nanocomposites for enhanced anticorrosion and flame retardant properties, Surf. Interfaces 70 (2025) 106850.

[39] S.T. Lazar, T.J. Kolibaba, J.C. Grunlan, Flame-retardant surface treatments, Nat. Rev. Mater. 5 (2020) 259.

[40] F. Carosio, L. Maddalena, J. Gomez, G. Saracco, A. Fina, Graphene oxide exoskeleton to produce self-extinguishing, nonignitable, and flame resistant flexible foams: a mechanically tough alternative to inorganic aerogels, Adv. Mater. Interfac. 5 (2018) 1801288.

[41] I. Lee, J. Jang, D. Choi, Y.T. Park, C. Cho, Layer-by-Layer assembly of TiO2 nanoparticle/poly (acrylic acid)/montmorillonite trilayer composite films as flame-retardant coatings, ACS Appl. Nano Mater. 7 (2024) 26843–26853.

[42] K.M. Holder, R.J. Smith, J.C. Grunlan, A review of flame retardant nanocoatings prepared using layer-by-layer assembly of polyelectrolytes, J. Mater. Sci. 52 (2017) 12923–12959.

[43] R.J. Smith, K.M. Holder, S. Ruiz, W. Hahn, Y. Song, Y.M. Lvov, J.C. Grunlan, Environmentally benign halloysite nanotube multilayer assembly significantly reduces polyurethane flammability, Adv. Funct. Mater. 28 (2018) 1703289.

[44] B. Palen, T.J. Kolibaba, J.T. Brehm, R. Shen, Y. Quan, Q. Wang, J.C. Grunlan, Clay-filled polyelectrolyte complex nanocoating for flame-retardant polyurethane foam, ACS Omega 6 (2021) 8016–8020.

[45] C. Vallés, R.J. Young, D.J. Lomax, I.A. Kinloch, The rheological behaviour of concentrated dispersions of graphene oxide, J. Mater. Sci. 49 (2014) 6311.

[46] J. Fu, J.B. Schlenoff, Driving forces for oppositely charged polyion association in aqueous solutions: enthalpic, entropic, but not electrostatic, J. Am. Chem. Soc. 138 (2016) 980–990.

[47] F. Fang, M. Li, J. Zhang, C.-S. Lee, Different strategies for organic nanoparticle preparation in biomedicine, ACS Mater. Lett. 2 (2020) 531–549.

[48] L.A. Kaledin, F. Tepper, Y. Vesga, T.G. Kaledin, Boehmite and akaganeite 1d and 2d mesostructures: synthesis, growth mechanism, ageing characteristics and surface nanoscale roughness effect on water purification, J. Nanomater. 2019 (2019) 9516156.

[49] N.M. Ashry, H.E. El Bahgy, A. Mohamed, N.H. Alsubhi, G.I. Alrefaei, N. Binothman, M. Alharbi, S. Selim, M.S. Almuhayawi, M.T. Alharbi, Evaluation of graphene oxide, chitosan and their complex as antibacterial agents and anticancer apoptotic effect on HeLa cell line, Front. Microbiol. 13 (2022) 922324.

[50] N.S. Zacharia, D.M. DeLongchamp, M. Modestino, P.T. Hammond, Controlling diffusion and exchange in layer-by-layer assemblies, Macromolecules 40 (2007) 1598–1603.

[51] Y-y Byun, J. Jang, M. Culebras, B.-S. Bae, J.S. Cho, Y.T. Park, C. Cho, Conformation-dependent thermoelectric power factor of multilayer nanocomposites, Appl. Surf. Sci. 594 (2022) 153483.

[52] C. Cho, F. Xiang, K.L. Wallace, J.C. Grunlan, Combined ionic and hydrogen bonding in polymer multilayer thin film for high gas barrier and stretchiness, Macromolecules 48 (2015) 5723–5729.

[53] C. Cho, K.L. Wallace, P. Tzeng, J.-H. Hsu, C. Yu, J.C. Grunlan, Outstanding low temperature thermoelectric power factor from completely organic thin films enabled by multidimensional conjugated nanomaterials, Adv. Energy Mater. 6 (2016) 1502168.

[54] M. Wang, Y.-J. Song, W. Jiang, F. Fornasiero, J.J. Urban, Mi Baoxia, Layer-by-layer assembly of nanosheets with matching size and shape for more stable membrane structure than nanosheet-polymer assembly, ACS Appl. Mater. Interfaces 16 (2024) 26568.

[55] H. Tang, S. Zhang, T. Huang, J. Zhang, B. Xing, Mechanisms of the aggregation of graphene oxide at high pH: roles of oxidation debris and metal adsorption, Environ. Sci. Technol. 55 (2021) 14639.

[56] X. Zhang, J. Chen, T. Jiang, J. Fu, X. Wu, H. Wang, Y. Sun, One-step synthesis of pseudo-boehmite by carbonation in a microchannel reactor, Chem. Eng. Technol. 46 (2023) 2175–2183.

[57] W. Gul, H. Alrobei, Effect of graphene oxide nanoparticles on the physical and mechanical properties of medium density fiberboard, Polymers 13 (2021) 1818.

[58] H. Sui, X. Ju, X. Liu, K. Cheng, Y. Luo, F. Zhong, Primary thermal degradation effects on the polyurethane film, Polym. Degrad. Stabil. 101 (2014) 109–113.

[59] L.G. Lage, Y. Kawano, Thermal degradation of biomedical polyurethanes—A kinetic study using high-resolution thermogravimetry, J. Appl. Polym. Sci. 79 (2001) 910–919.

[60] J.R. Beryl, J.R. Xavier, Halloysite for clay-polymer nanocomposites: effects of nanofillers on the anti-corrosion, mechanical, microstructure, and flame-retardant properties-a review, J. Mater. Sci. 58 (2023) 10943–10974.

[61] S. Zhang, F. Chu, Z. Xu, Y. Zhou, Y. Qiu, L. Qian, Y. Hu, B. Wang, W. Hu, The improvement of fire safety performance of flexible polyurethane foam by highly-efficient PNS elemental hybrid synergistic flame retardant, J. Colloid Interface Sci. 606 (2022) 768–783.

[62] P. McKeen, Z. Liao, Pyrolysis model for predicting the fire behavior of flexible polyurethane foam, in: Building Simulation, Springer, 2019, pp. 337–345.

[63] I. Lee, S.J. Kim, Y.Y. Byun, I. Chang, Y.-W. Ju, Y.T. Park, J. Jang, C. Cho, High flame retardancy enabled by dual clays-based multilayer nanocomposites, Prog. Org. Coating 183 (2023) 107784.

[64] Y.S. Kim, R. Harris, R. Davis, Innovative approach to rapid growth of highly clay-filled coatings on porous polyurethane foam, ACS Macro Lett. 1 (2012) 820–824.

[65] J.R. Xavier, Investigation of anticorrosion, flame retardant and mechanical properties of polyurethane/GO nanocomposites coated AJ62 Mg alloy for aerospace/automobile components, Diam. Relat. Mater. 136 (2023) 110025.

[66] J.R. Xavier, S.P. Vinodhini, Improved anticorrosion, flame retardant and mechanical behaviors of multifunctional polyurethane nanocomposite coatings for industrial applications, Polym. Degrad. Stabil. 213 (2023) 110370.

[67] D. Patra, P. Vangal, A. CainA, C. Cho, O. Regev, J.C. Grunlan, Inorganic nanoparticle thin film that suppresses flammability of polyurethane with only a single electrostatically-assembled bilayer, ACS Appl. Mater. Interfaces 6 (2014) 16903–16908.

[68] J.N. Gavgani, H. Adelnia, M.M. Gudarzi, Intumescent flame retardant polyurethane/reduced graphene oxide composites with improved mechanical, thermal, and barrier properties, J. Mater. Sci. 49 (2014) 243–254.

[69] R. Wang, D. Zhuo, Z. Weng, L. Wu, X. Cheng, Y. Zhou, J. Wang, B. Xuan, A novel nanosilica/graphene oxide hybrid and its flame retarding epoxy resin with simultaneously improved mechanical, thermal conductivity, and dielectric properties, J. Mater. Chem. A 3 (2015) 9826–9836.